Available online at www.sciencedirect.com

ScienceDirect

Materials Today: Proceedings 1 (2014) 25 – 34

materialstoday: PROCEEDINGS

www.materialstoday.com/proceedings

The 1st International Joint Mini-Symposium on Advanced Coatings between Indiana University-Purdue University Indianapolis and Changwon National University

# First principles study of thermodynamic properties of lanthanum zirconate

Xingye Guo, Jing Zhang*

*Department of Mechanical Engineering, Indiana University-Purdue University Indianapolis, Indianapolis, IN 46202, USA*

**Abstract**

Lanthanum zirconia ($La_2Zr_2O_7$) has become an advanced thermal barrier coating material due to its low thermal conductivity and high temperature stability. In this work, the first principles calculations were used to study the thermodynamic properties of the material. Lattice parameters, bulk and shear modulus, and specific heat of $La_2Zr_2O_7$ were calculated by means of density functional theory (DFT). Hydrostatic pressure-dependent elasticity constants and bulk modulus were also studied. The thermal conductivity was calculated based on the Fourier's law. The calculated properties are in excellent agreement with the experimental and calculation results in literature.


Selection and Peer-review under responsibility of the Chairs of The 1st International Joint Mini-Symposium on Advanced Coatings between Indiana University-Purdue University Indianapolis and Changwon National University, Indianapolis.

*Keywords:* Lanthanum zirconate; first principles calculations; thermal property; mechnical property; thermodynamic property

* Corresponding author. Tel.: +0-317-278-7186; fax: +0317-274-9744.
*E-mail address:* jz29@iupui.edu


Selection and Peer-review under responsibility of the Chairs of The 1st International Joint Mini-Symposium on Advanced Coatings between Indiana University-Purdue University Indianapolis and Changwon National University, Indianapolis.
doi:10.1016/j.matpr.2014.09.006

## 1. Introduction

Pyrochlore $A_2B_2O_7$ (A and B are both metals) has drawn interests recently due to its potential application in thermal barrier coating applications. The B element in $A_2B_2O_7$ typically is a transition metal or a post transition metal with variable oxidation states, and the A element typically is a rare earth element or an element with inert single-pair of electrons [1]. As a typical pyrochlore structure, $La_2Zr_2O_7$ exhibits lower thermal conductivity and good thermal stability at high temperatures. So it is recently widely proposed for thermal barrier coating (TBC) applications. Thermal barrier coatings are multi-layered material systems deposited on blades of gas turbine engine to thermally insulate them and to protect them against hot and corrosive gas streams [2].

Typical structure of a thermal barrier coating includes four layers: superalloy substrate, bond coat,thermally grown oxide (TGO), and ceramic top coat. The nickel and cobalt based superalloy substrate is air cooled from the inside. The bond-coat is an oxidation-resistant layer which also has a close thermal expansion coefficient with the substrate, so that there is less stress due to differential thermal expansions. Typically bond coat consists of a NiCoCrAlY alloy with a thickness of 100–300 μm applied on the substrate, which is deposited by air plasma spraying (APS) or electron-beam physical vapor deposition (EB-PVD) methods. At high temperature operation conditions, the bond coat is inevitably oxidized to form a thermally grown oxide layer with a 1-10 μm thickness, which is located between the bond coat and the ceramic top coat. Typically TGO is formed as an $\alpha$-$Al_2O_3$ layer which can be an excellent oxygen diffusion barrier to protect the bond-coat from further oxidation [2, 3]. The ceramic top coat is a low thermal conductivity ceramic material with a typical thickness of 100–400 μm deposited by APS or EB-PVD methods. 6%-8% yttria-stabilized zirconia (YSZ) is now widely used as top coat. YSZ top coat has the thermal conductivity about 2.0-2.3 W/m/K at 1000 $^oC$ [4, 5] at fully dense. Whereas $La_2Zr_2O_7$ top coat has a thermal conductivity about 1.55W/m/K at 1000 $^oC$ at fully dense [6]. $La_2Zr_2O_7$ has a lower thermal conductivity than YSZ. And $La_2Zr_2O_7$ has no phase change while heated from room temperature to its melting point [7]. So it is thermally stable during the heating and cooling stages. $La_2Zr_2O_7$ can be a better contestant for advanced thermal barrier coating.

Vassen *et al* [6, 8-10] experimentally studied the properties of $La_2Zr_2O_7$, including the thermal conductivity, specific heat at constant pressure, Young's modulus and thermal expansion coefficient [6]. YSZ and $La_2Zr_2O_7$ were comparatively studied [9]. The only disadvantage of $La_2Zr_2O_7$ is that it has a relatively low thermal expansion coefficient. Through doping, the thermal expansion coefficient of $La_2Zr_2O_7$ can be increased [9]. The thermal stability of $La_2Zr_2O_7$ was studied using long-term annealing at 1400$^oC$ and thermal cycling test. $La_2Zr_2O_7$ coating had a high phase stability against thermal treatment. But the thermal cycling lifespan needed to be improve by increasing the $La_2O_3$ content in the starting powder or doping elements into $La_2Zr_2O_7$ [10].

Zhu *et al* [11] studied the advanced thermal environmental barrier coating (TEBC), which includes $La_2Zr_2O_7$, $HfO_2$-$Y_2O_3$, and Gd/Yb doped $La_2Zr_2O_7$. TEBCs have a better high-temperature stability up to 1650 $^oC$ (3000 $^oF$) and a lower thermal conductivity. They are more resistant to sintering and thermal stress under a high-heat-flux environment and severe thermal cycling conditions. The thermal conductivity was measured for a dense $La_2Zr_2O_7$ was 2.1-2.8W/m/K from 800-1400 $^oC$, which is much higher than Vassen's work [6].

Xiang and Huang[12] studied the phase structure and thermal properties of co-doped $La_2Zr_2O_7$, which included $La_2Zr_2O_7$, $(La_{0.7}Yb_{0.3})_2(Zr_{0.7}Ce_{0.3})_2O_7$, and $(La_{0.2}Yb_{0.8})_2(Zr_{0.7}Ce_{0.3})_2O_7$. The phase structure was identified by X-ray diffraction. The thermal conductivity and thermal expansion coefficient were measured. The results showed that the co-doped $(La_{0.7}Yb_{0.3})_2(Zr_{0.7}Ce_{0.3})_2O_7$, and $(La_{0.2}Yb_{0.8})_2(Zr_{0.7}Ce_{0.3})_2O_7$ have a higher thermal expansion coefficient and lower thermal conductivity than $La_2Zr_2O_7$.

Liu [13] calculated the elastic constant, Young's modulus and thermal conductivity of $La_2Zr_2O_7$ by first principles theory and pseudo-potential total energy method. From the results of elastic stiffness, the anisotropic Young's modulus on (0 1 1) plane was calculated. The volume and relative bond ratio as a function of hydrostatic pressure were also computed. By examining the bond length and applied pressure, the La-O bonds were shown to be weaker than the Zr-O bond in $La_2Zr_2O_7$.

Chartier [14] used molecular dynamics to calculate the specific heat of $La_2Zr_2O_7$ at constant pressure, and studied the formation energy of point defects. A displacement cascade in $La_2Zr_2O_7$ crystal was investigated. The result showed that in pristine $La_2Zr_2O_7$ the primary radiation induced damage was a transition towards the disordered fluorite state.

Although there are several previous studies on $La_2Zr_2O_7$, there is a lack of fundamental understanding the thermodynamic properties of the material, which hinders its application in thermal barrier coating. This work will focus on the thermodynamic properties and mechanical properties using the first principles calculations.

## 2. Method

### *2.1. Density function theory*

The calculations in this study were based on the first principles method using the density functional theory (DFT), described by the Schrödinger equation. Density function theory (DFT) was initiated as an alternate approach to solve the Schrödinger equation. DFT expresses the theory of electronic structure by electron density distribution *n(r)* rather than the many-electron wave function[15]. DFT uses the Kohn-Sham equation to express the density distribution [16-19]:

$$[-\frac{h^2}{2m}\nabla^2 + V(r) + V_H(r) + V_{XC}(r)]\cdot\psi_{nk}(r) = \varepsilon_{nk}\psi_{nk}(r) \tag{1}$$

where $m$ is electron mass, $h$ is Planck's constant, $\Psi_{nk}(r)$ is electron wave function, $r$ is the coordinate of electron, $V(r)$ is a potential energy that defines the interaction between an electron and the collection of atomic nuclei, $V_H(r)$ is the Hartree potential which defines the Coulomb repulsion between electrons, $V_{XC}(r)$ is the functional derivative of the exchange-correlation potential. $V_H$ and $V_{XC}$ can be expressed:

$$V_H(r) = e^2\int\frac{n(r')}{|r-r'|}d^3r' \qquad V_{xc}(r) = \frac{\delta E_{XC}(r)}{\delta n(r)} \qquad n(r) = \sum_{nk}^{\#of\_e}|\psi_{nk}(r)|^2 \tag{2}$$

### *2.2. Crystal structure*

$La_2Zr_2O_7$ is a pyrochlore crystal ($A_2B_2O_6O'$), which has a cubic crystal system in space group $Fd\bar{3}m$. If the origin is chosen at the B site, then atom A occupies the 16d position (1/2, 1/2, 1/2), atom B resides at 16c position (0, 0, 0), O1which is O' atom in chemical formula locates at 8b positions (3/8,3/8,3/8), while O2 which stands for $O_6$ in $A_2B_2O_6O'$ locates at 48f positions (x, 1/8, 1/8)[20]. The A and B form a face-centered cubic. For $La_2Zr_2O_7$ conventional cell, the La atom corresponds to A site and Zr atom corresponds to B site.

The conventional cell has 16 La atoms, 16 Zr atoms and 56 O atoms. It is necessary to reduce the atoms by converting it into a primitive cell, which has 4 La atoms 4 Zr atoms and 14 O atoms. Figure 1 shows the conventional cell and the primitive cell of the $La_2Zr_2O_7$ crystal model.

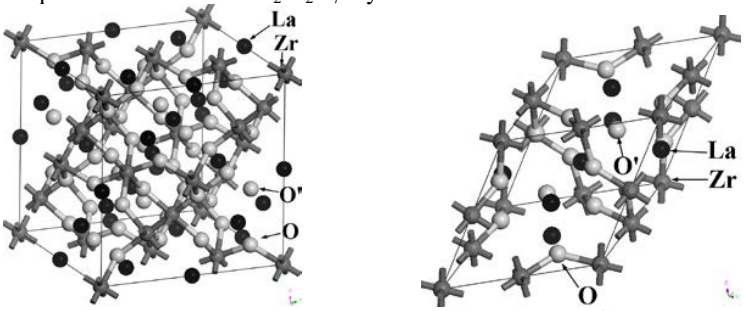


(a) (b)

Fig. 1 $La_2Zr_2O_7$ (a) Conventional cell, and (b) primitive cell

### *2.3. Geometry optimization*

Geometry optimization was conducted to find the equilibrium lattice parameter at the minimum energy position [21]. The optimized lattice parameter using CASTEP was 10.73Å for the conventional cell, and 7.59 Å for the primitive cell.

Figure 2 shows the free energy as a function of lattice parameter using VASP. The optimized lattice parameter was 10.875 Å, where the corresponding free energy was -803.749eV. The calculated lattice parameter is very close to previous study using CASTEP, 10.73 Å [13], and 10.802 Å using XRD analysis[22].

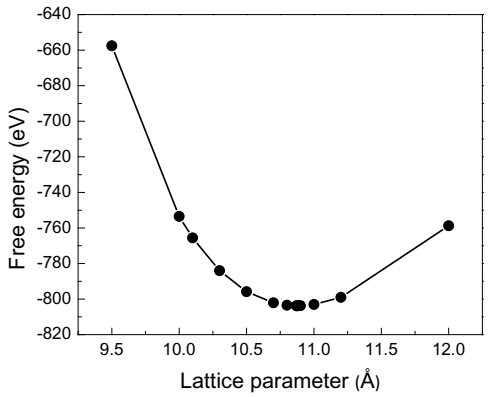


Fig. 2 Geometry optimization of energy minimization as a function of lattice parameter.

## 3. Results and discussion

### *3.1. Energy and specific heat of $La_2Zr_2O_7$*

The calculated free energy, enthalpy and entropy as a function of temperature are shown in Figure 3. The entropy increased with increasing temperature, due to increased configurations. The enthalpy increased slowly and the total free energy decreased as the temperature increased. The enthalpy exhibited the increased thermal energy. Since the Gibbs free energy equals to the enthalpy minus the product of temperature and entropy, it is reasonable that the free energy decreased as temperature increased.

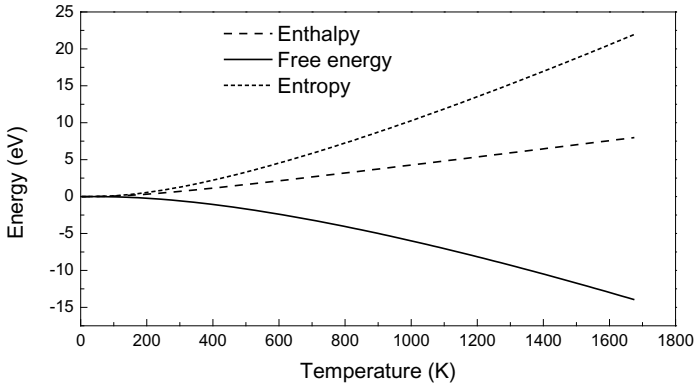


Fig. 3 Free energy, enthalpy and entropy as a function of temperature

The calculated specific heat (Cp) at constant pressure is shown in Figure 4 in the temperature range of 0 K to 1600 K. It should be noted that the low temperature data are very difficult to measure by experiment. The value of specific heat increased as the temperature increased. When the temperature reached above 600 K, the specific heat reached a plateau. The specific heat values were 0.4~0.467 J/g/K from 600 K to 1600 K. As shown in Figure 4, the comparison with experimental data from Vassen's group [6, 8] and calculation from Chartier [14] is excellent.

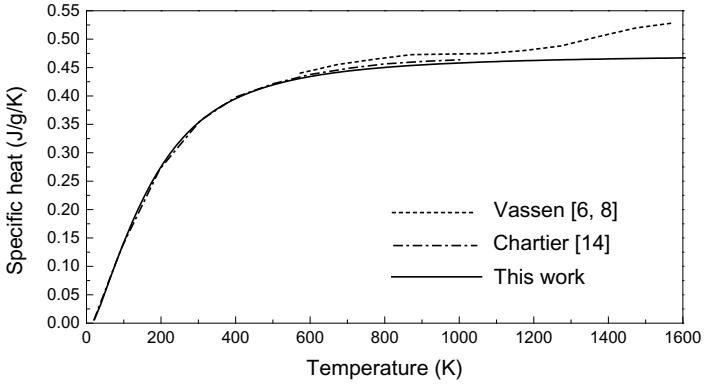


Fig. 4 Specific heat at constant pressure as a function of temperature.

### *3.2. Elastic properties of $La_2Zr_2O_7$*

The elastic constants of a material describe its response to an applied stress or, conversely, the stress required to maintain a given deformation. Both stress and strain have three tensile and three shear components, giving six components in total. The linear elastic constants form a 6 × 6 symmetric matrix, having 27 different components:

$$\begin{bmatrix} \varepsilon_x \\ \varepsilon_y \\ \varepsilon_z \\ \gamma_x \\ \gamma_y \\ \gamma_z \end{bmatrix} = \begin{Bmatrix} C_{11} & C_{12} & C_{13} & C_{14} & C_{15} & C_{16} \\ C_{21} & C_{22} & C_{23} & C_{24} & C_{25} & C_{26} \\ C_{31} & C_{32} & C_{33} & C_{34} & C_{35} & C_{36} \\ C_{41} & C_{42} & C_{43} & C_{44} & C_{45} & C_{46} \\ C_{51} & C_{52} & C_{53} & C_{54} & C_{55} & C_{56} \\ C_{61} & C_{62} & C_{63} & C_{64} & C_{65} & C_{66} \end{Bmatrix} \begin{bmatrix} \sigma_x \\ \sigma_y \\ \sigma_z \\ \tau_x \\ \tau_y \\ \tau_z \end{bmatrix} \tag{3}$$

But for $La_2Zr_2O_7$ structure, there are only three independent elastic constant $C_{11}$, $C_{12}$, and $C_{44}$ due to cubic structure. Table 1 shows the elastic constants, the bulk modulus and the shear modulus, which are in agreement with previous calculation [13].

Table 1. Elastic constants, bulk modulus and shear modulus of $La_2Zr_2O_7$.

| An example of a column heading | C11 (GPa) | C12 (GPa) | C44 (GPa) | Bulk modulus (GPa) | Shear modulus (GPa) |
|---|---|---|---|---|---|
| This work | 289.847 | 124.755 | 100.431 | 179.785 | 93.277 |
| Liu's work (CASTEP) [13] | 289 | 124 | 100 | 179 | 93 |

The bulk modulus and lattice parameter as a function of hydrostatic pressure are plotted in Figure 5. The bulk modulus increased and the lattice parameter decreased with increasing pressure.

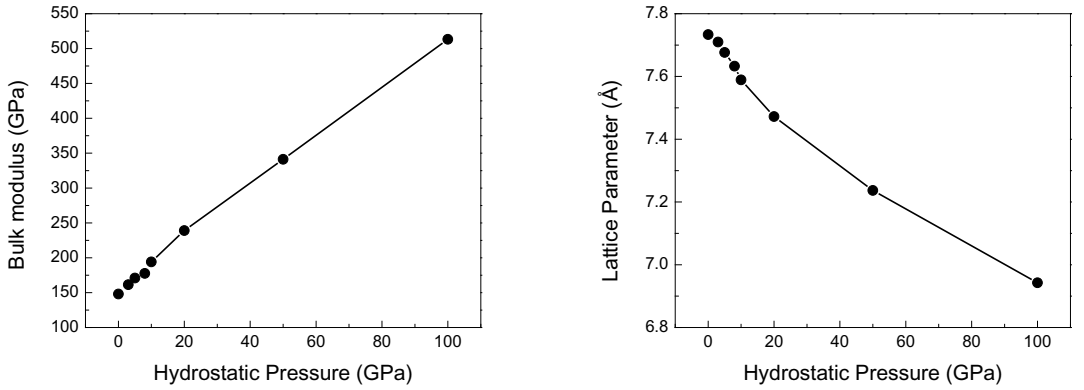


(a) (b)

Fig. 5 (a) Bulk modulus and (b) lattice parameter as a function of hydrostatic pressure

The volume ratio and the relative bond length as a function of hydrostatic pressure are shown in Figure 6. It is clear that the volume ratio and the relative bond length decreased as the pressure increased, as expected [13].

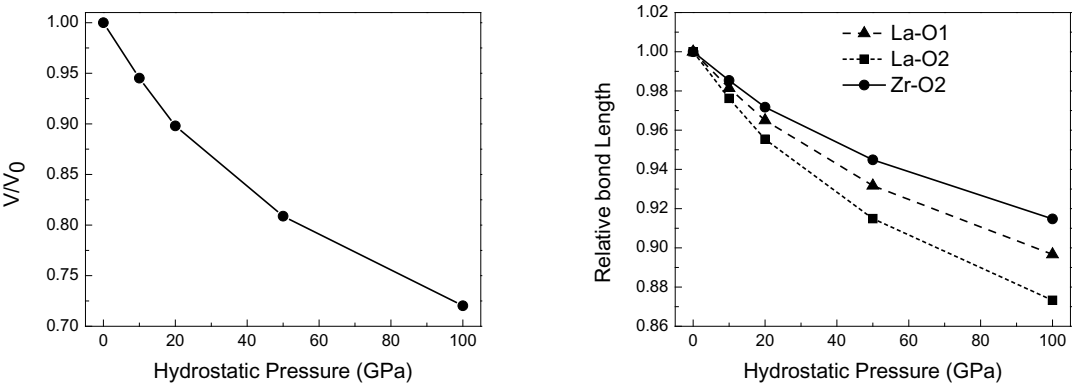


(a) (b)

Fig. 6 (a) Volume ratio and (b) relative bond length as a function of hydrostatic pressure

When the three independent elastic constant $C_{11}$, $C_{12}$, and $C_{44}$ in all direction are available, the anisotropic characteristics of $La_2Zr_2O_7$ can be calculated using the Zener anisotropy ratio [23]:

$$Z = \frac{2C_{44}}{C_{11} - C_{12}} \tag{4}$$

For Z=1 the material is isotropic. When Z<1 the maximum Young's modulus is located in the <1 0 0> direction. When Z>1, the maximum Young's modulus is located in the <1 1 1> direction [23]. Using the elastic constants in

Table 1, the calculated Z for $La_2Zr_2O_7$ was 1.21, which is greater than 1. So the maximum Young's modulus of $La_2Zr_2O_7$ is in <1 1 1> direction.

The anisotropic Young's modulus *E* for materials of cubic symmetry is:

$$\frac{1}{E}=\frac{l^4+m^4+n^4}{E_0}+\frac{2\left(m^2n^2+n^2l^2+l^2m^2\right)}{F_0} \tag{5}$$

where $\frac{1}{E_0}=\frac{C_{11}+C_{12}}{(C_{11}-C_{12})(C_{11}+2C_{12})}$ and $\frac{2}{F_0}=\frac{-2C_{12}}{(C_{11}-C_{12})(C_{11}+2C_{12})}+\frac{1}{C_{44}}$ (6)

where *l*, *m*, and *n* are directional cosines. In this work, the anisotropic Young's modulus on (0 1 1) plane was calculated, because both of the maximum Young's modulus direction [1 1 1] and the minimum Young's modulus direction [1 0 0] are located in this plane. The directional cosines of $La_2Zr_2O_7$ crystal in (0 1 1) plane can be calculated [23]:

$$l=\cos\theta,\quad m=\frac{\sin\theta}{\sqrt{2}}\ \text{and}\ \ n=\frac{\sin\theta}{\sqrt{2}} \tag{7}$$

where $\theta$ is the angle in the (0 1 1) plane measured from the [1 0 0] direction to the [1 1 0] direction.

Anisotropic Young's modulus of $La_2Zr_2O_7$ crystal on (0 1 1) plane is plotted in Figure 7. The calculated maximum value of anisotropic Young's modulus was 253.995 GPa in [1 1 1] direction, while the minimum value was 214.768 GPa, located in [1 0 0] direction. Moreover, the Young's modulus in [0 1 1] direction was 242 GPa.

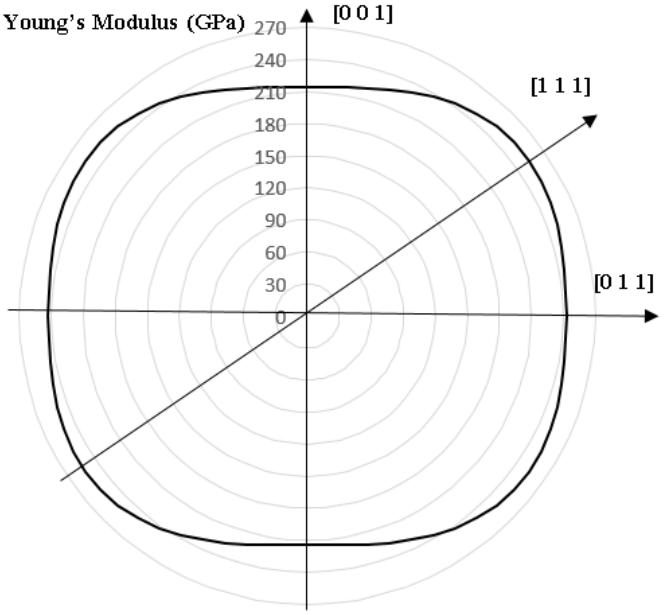


Fig. 7 Anisotropic Young's modulus on (0 1 1) plane

### *3.3. Thermal conductivity of $La_2Zr_2O_7$*

A super cell which contains 1×1×20 conventional cells was used to calculate thermal conductivity (Figure 8a). The total length of the super cell was 218.739038Å. Thermostat decay constant was set 0.1 s, time step 5s/step and 300 steps. The decay constant is the time required for the temperature reaches to half of the difference between the initial and target temperatures. Fig. 8b shows the calculate temperature contour.

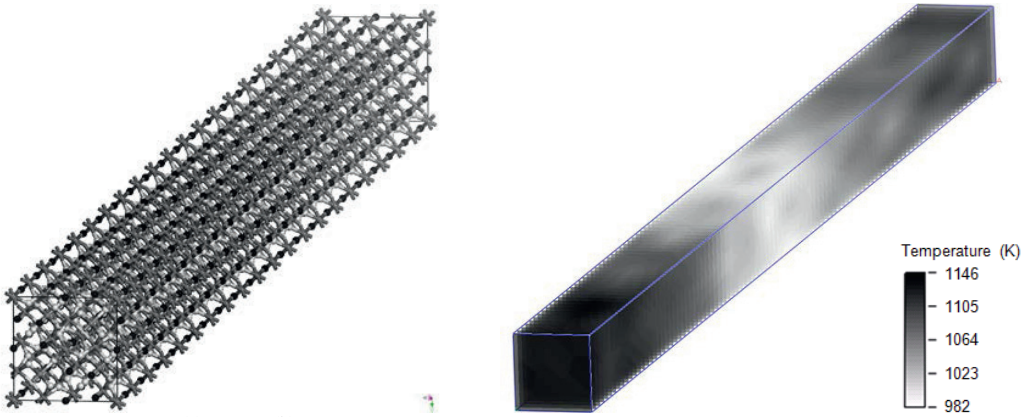


Fig. 8 (a) supper cell and (b) temperature contour

Figure 9 shows the calculated thermal conductivity history. The conductivity became stable after 800 ps. The calculated thermal conductivity is about 1.2 W/m/K at the initial temperature of 1000 $^{o}$C. Comparing with the experiment value 1.55 W/m/K at 1000$^{o}$C [8], the result of this work is in good agreement.

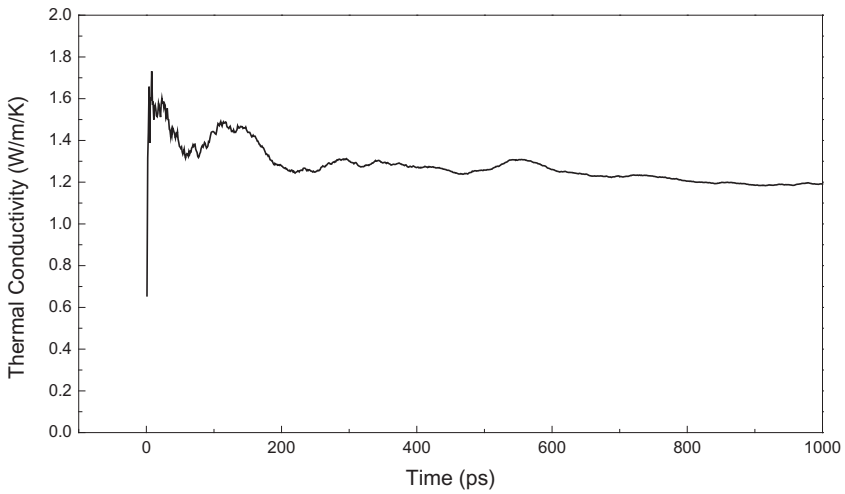


Fig. 9 Evolution of the calculated thermal conductivity

Figure 10 shows the temperature distribution along the super cell. A smooth temperature distribution was observed, which is consistent with Figure 8b. Figure 11 shows the energy flux evolution, which in agreement with Figure 9. From these figures, it can be concluded that the calculated thermal conductivity was converged.

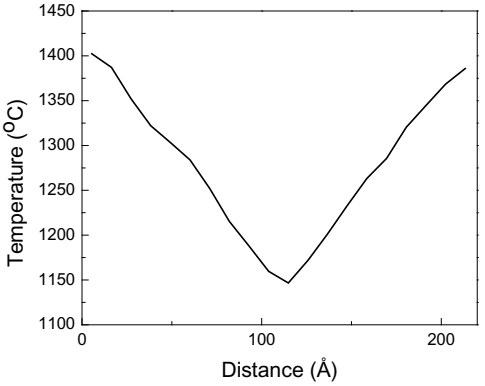


Fig. 10 Temperature distribution as function of distance

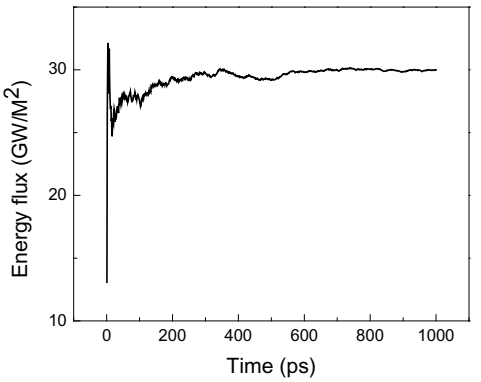


Fig. 11 Energy flux evolution

## 4. Conclusions

First principles calculations have been used to investigate the thermodynamic and mechanical properties of $La_2Zr_2O_7$. The elastic constant, anisotropic Young's modulus on (0 1 1) plane, volume ratio with respect to the hydrostatic pressure, specific heat and the thermal conductivity, were calculated. Specifically, it can draw the following conclusions:

(a) The calculated specific heat at constant pressure was 0.4-0.46 J/g/K in a temperature range of 600~1600K;
(b) The bulk modulus increased and the lattice parameters decreased as increasing hydrostatic pressure;
(c) The anisotropic Young's modulus reached its maximum value of 254 GPa in [1 1 1] direction on (0 1 1) plane;
(d) The calculated thermal conductivity value was around 1.2 W/m/K.

## Acknowledgements

The authors would like to acknowledge the financial support provided by DOE (Grant No. DE-FE0008868, program manager Richard Dunst).

## References

1. Subramanian, M.A., G. Aravamudan, and G.V. Subba Rao, *Oxide pyrochlores — A review.* Progress in Solid State Chemistry, 1983. **15**(2): p. 55-143.
2. Weber, S.B., et al., *Lanthanum zirconate thermal barrier coatings deposited by spray pyrolysis.* Surface and Coatings Technology, 2013. **227**(0): p. 10-14.

3. Padture, N.P., M. Gell, and E.H. Jordan, *Thermal Barrier Coatings for Gas-Turbine Engine Applications.* Science, 2002. **296**(5566): p. 280-284.
4. Schlichting, K.W., N.P. Padture, and P.G. Klemens, *Thermal conductivity of dense and porous yttria-stabilized zirconia.* Journal of Materials Science, 2001. **36**(12): p. 3003-3010.
5. Hasselman, D.P.H., et al., *Thermal diffusivity and conductivity of dense polycrystalline $ZrO_2$ ceramics: a survey.* American Ceramic Society Bulletin, 1987. **66**(5): p. 799-806.
6. Vassen, R., et al., *Zirconates as New Materials for Thermal Barrier Coatings.* Journal of the American Ceramic Society, 2000. **83**(8): p. 2023-2028.
7. Zhou, H., et al., *Preparation and thermophysical properties of CeO2 doped La2Zr2O7 ceramic for thermal barrier coatings.* Journal of Alloys and Compounds, 2007. **438**(1-2): p. 217-221.
8. Lehmann, H., et al., *Thermal Conductivity and Thermal Expansion Coefficients of the Lanthanum Rare-Earth-Element Zirconate System.* Journal of the American Ceramic Society, 2003. **86**(8): p. 1338-1344.
9. Cao, X.Q., R. Vassen, and D. Stoever, *Ceramic materials for thermal barrier coatings.* Journal of the European Ceramic Society, 2004. **24**(1): p. 1-10.
10. Cao, X.Q., et al., *Thermal Stability of Lanthanum Zirconate Plasma-Sprayed Coating.* Journal of the American Ceramic Society, 2001. **84**(9): p. 2086-2090.
11. Zhu, D., et al., *Advanced Oxide Material Systems for 1650 $^oC$ Thermal/Environmental Barrier Coating Applications*, 2004, National Aeronautics Space Administration, John H. Glenn Research Center.
12. Xiang, J., et al., *Phase structure and thermophysical properties of co-doped La2Zr2O7 ceramics for thermal barrier coatings.* Ceramics International, 2012. **38**(5): p. 3607-3612.
13. Liu, B., et al., *Theoretical elastic stiffness, structure stability and thermal conductivity of La2Zr2O7 pyrochlore.* Acta Materialia, 2007. **55**(9): p. 2949-2957.
14. Chartier, A., et al., *Atomistic modeling of displacement cascades in $La_2Zr_2O_7$ pyrochlore.* Physical Review B, 2003. **67**(17): p. 174102.
15. Kohn, W., *Nobel Lecture: Electronic structure of matter—wave functions and density functionals.* Reviews of Modern Physics, 1999. **71**(5): p. 1253-1266.
16. Hohenberg, P. and W. Kohn, *Inhomogeneous electron gas.* Physical review, 1964. **136**(3B): p. B864.
17. Kohn, W. and L.J. Sham, *Self-Consistent Equations Including Exchange and Correlation Effects.* Physical Review, 1965. **140**(4A): p. A1133-A1138.
18. Kohn, W., *Density functional/Wannier function theory for systems of very many atoms.* Chemical Physics Letters, 1993. **208**(3–4): p. 167-172.
19. Sholl, D. and J.A. Steckel, *Density functional theory: a practical introduction*2011: John Wiley & Sons.
20. Xiao, H.Y., et al., *Theoretical investigation of structural, energetic and electronic properties of titanate pyrochlores.* Journal of Physics: Condensed Matter, 2007. **19**(34): p. 346203.
21. Barsoum, M.W., *Fundamentals of ceramics*2002: CRC Press.
22. Tabira, Y., et al., *Systematic Structural Change in Selected Rare Earth Oxide Pyrochlores as Determined by Wide-Angle CBED and a Comparison with the Results of Atomistic Computer Simulation.* Journal of Solid State Chemistry, 2000. **153**(1): p. 16-25.
23. Ingel, R.P. and D.L. Iii, *Elastic Anisotropy in Zirconia Single Crystals.* Journal of the American Ceramic Society, 1988. **71**(4): p. 265-271.